

# Liquid-organic time projection chamber for detecting low energy antineutrinos

---

**T. Radermacher,<sup>a,b,1</sup> J. Bosse,<sup>a,b</sup> S. Friedrich,<sup>a</sup> M. Götsche,<sup>a,b</sup> S. Roth<sup>a</sup> and G. Schwefer<sup>a,b</sup>**

<sup>a</sup>*III. Physikalisches Institut B, RWTH Aachen University  
Sommerfeldstraße 16, 52074 Aachen, Germany*

<sup>b</sup>*Aachen Institute for Advanced Study in Computational Engineering Science (AICES), RWTH Aachen University,  
Schinkelstraße 2, 52056 Aachen, Germany*

*E-mail:* [radermacher@physik.rwth-aachen.de](mailto:radermacher@physik.rwth-aachen.de)

**ABSTRACT:** The MeV region of antineutrino energy is of special interest for physics research and for monitoring nuclear nonproliferation. Whereas liquid scintillation detectors are typically used to detect the Inverse Beta Decay (IBD), it has recently been proposed to detect it with a liquid-organic Time Projection Chamber, which could allow a full reconstruction of the particle tracks of the IBD final state. We present the first comprehensive simulation-based study of the expected signatures. Their unequivocal signature could enable a background-minimized detection of electron antineutrinos using information on energy, location and direction of all final state particles. We show that the positron track reflects the antineutrino's vertex. It can also be used to determine the initial neutrino energy. In addition, we investigate the possibility to reconstruct the antineutrino direction on an event-by-event basis by the energy deposition of the neutron-induced proton recoils. Our simulations indicate that this could be a promising approach which should be further studied through experiments with a detector prototype.

**KEYWORDS:** Liquid detectors; Time projection Chambers (TPC); Neutrino detectors; Search for radioactive and fissile materials

ARXIV EPRINT: [2203.01090](https://arxiv.org/abs/2203.01090)

---

<sup>1</sup>Corresponding author.

---

## Contents

<b>1</b>	<b>Introduction</b>	<b>1</b>
<b>2</b>	<b>Antineutrinos from Nuclear Waste</b>	<b>3</b>
<b>3</b>	<b>Liquid-organic time projection chamber</b>	<b>4</b>
<b>4</b>	<b>Simulation setup and event generation</b>	<b>5</b>
<b>5</b>	<b>Inverse beta decay signature in a LOr-TPC</b>	<b>6</b>
<b>6</b>	<b>Investigations on the reconstruction of the antineutrino direction</b>	<b>9</b>
<b>7</b>	<b>Conclusion and Outlook</b>	<b>12</b>
<b>A</b>	<b>Initial study for monitoring a geological repository with a liquid-organic TPC</b>	<b>12</b>

---

## 1 Introduction

Thanks to important advances in detector technology and analysis techniques, experimental neutrino research has become a field of precision physics that continues to push boundaries of sensitivity and accessible energy. Over the last years, the MeV region of neutrino energy has been of particular interest, e.g. for the investigation of reactor, solar and geoneutrinos.

In addition, the energy domain below 10 MeV can be useful for nuclear monitoring purposes where antineutrinos are produced by  $\beta$ -decaying fission products. With regard to reactors, a number of studies, for instance [1, 2], have examined antineutrino monitoring to observe whether reactors are operational, or even to deduce parameters such as fuel burnup or power. In such applications, detectors would typically be placed in close vicinity to the reactor building. Another project [3] looks at the potential for antineutrino monitoring to detect undeclared reactors from some distance, a significantly more challenging task.

For nuclear waste, both in interim storage facilities and in future geological repositories, verification activities are required to control the non-diversion of spent fuel which contains plutonium. For the case that other verification techniques fail, antineutrino monitoring could act as a redundancy without common failure modes [4, 5]. The main challenge will be a low neutrino flux intensity.

Antineutrinos in the MeV-energy range can be detected via their interaction with a proton producing a neutron and a positron, which had also been used for the discovery of the neutrino. This reaction, called Inverse Beta Decay (IBD), has the advantage of a clear final state signature consisting of a prompt signal of the two 511 keV photons from the positron annihilation and a delayed photon signal from the absorption of the neutron in a nucleus. Selecting this event signature reduces background sources to a large extent.

Typically, organic scintillation detectors are used to measure the energy depositions of the prompt and delayed signals. For high fluxes, e.g. directly in front of a nuclear reactor, no extensive shielding is necessary [6, 7]. It has been shown that using IBD is also effective enough for measuring moderate neutrino fluxes in some distance to the reactors in neutrino oscillation experiments [8–10], though requiring much larger detectors and a more significant overburden that shields against cosmic radiation. Lastly, this method even allows the measurement of the very small flux of geoneutrinos that has been successfully performed by Borexino [11]. Here, not only very large amounts of overburden are necessary, but also further measures against background sources such as veto counters and shielding against intrinsic radiation of the surrounding rocks are required. In addition, the scintillator needs to be of high purity to avoid radioactive decays inside of the detector.

These elaborate precautions against background are needed due to the fact that in liquid scintillation detectors the final state of the IBD reaction is not reconstructed in detail. Instead, the measurement uses only the three following observables of the event: The prompt energy from the positron annihilation, the delayed energy caused by the neutron absorption and the time between both energy depositions. For instance, IBD events cannot be distinguished from events involving electrons and neutrons (e.g. from cosmogenically produced  ${}^9\text{Li}$  or  ${}^8\text{He}$ ) as annihilation photons cannot be identified, because the prompt energy of the event, the kinetic energy of positron and the energy from the positron annihilation, is measured as a whole.

In this paper, we propose a different detection method that could have the benefit of strongly reduced background, namely detecting IBD events using the tracking capabilities of a Time Projection Chamber (TPC) to fully reconstruct the ionization of each particle of the IBD final state. This is to be achieved using an organic liquid. It contains sufficient free protons to serve as a target for IBD reactions, as has already been proposed by previous studies [12, 13]. Specifically, in each IBD event one could seek to identify the initial positron track, the energy depositions of the two annihilation photons and of the delayed photon emitted due to the neutron absorption by a nucleus. Furthermore, ionization clusters induced by the neutron scattering off the nuclei of the detector material might be detectable.

Reconstructing the tracks and showers from the original individual hits could provide information about the energy, the location and, with limitations, also the direction of the final state particles. The unequivocal signature of an IBD final state would enable background-minimized detection of electron antineutrinos. This would then allow to use the IBD antineutrino detection also for sources with smaller neutrino fluxes like nuclear waste or geoneutrinos and also in locations with less or even without any overburden.

An additional benefit could be the access to information on the initial direction of the detected antineutrino. Liquid scintillation detectors have also looked for final state variables that contain information on the antineutrino direction [14]. However, these measurements allow only a poor reconstruction. The results are based on the statistical analysis of a large number of antineutrino events. By using the final state as measured with a TPC, the variables sensitive to the antineutrino direction could be reconstructed with higher precision. New variables like the position of the neutron absorption or even neutron scattering with respect to the positron track become available and could be included in the reconstruction of the antineutrino direction. Hence, the antineutrino direction could possibly be measured on an event-by-event basis. If the directionality information can be improved sufficiently by this technique, one could be able to discriminate antineutrino

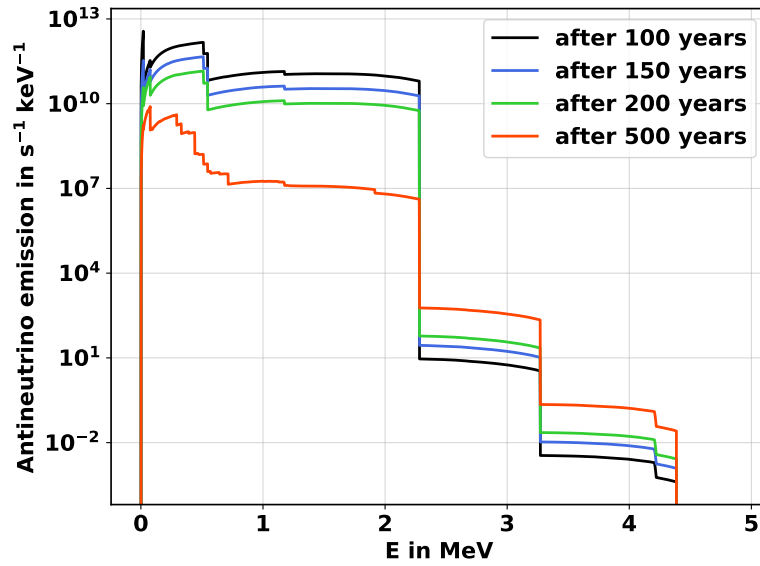


**Figure 1.** Energy spectra of antineutrinos emitted from one fuel assembly of a simulated PWR reactor with a burnup of 55 MWd/kg and enrichment of 4%.

background from the signal, e.g. reactor antineutrino background when measuring nuclear waste. The same holds for the determination of the distribution of radioactive nuclides within the rock formations when studying geoneutrinos.

In this paper, we present results of the first comprehensive simulation-based study of the expected IBD signatures in a liquid-organic TPC. The goal is to identify opportunities and challenges for their reconstruction. We use the example of antineutrinos emitted from nuclear waste as they present a significant challenge due to their energies reaching barely above the IBD detection threshold. Particular emphasis is placed on examining whether the antineutrino direction might indeed be reconstructable, as this would clearly be the most challenging reconstruction task.

## 2 Antineutrinos from Nuclear Waste

In the first few hundreds of years, the dominant radioactivity in nuclear waste comes from the  $\beta$ -decaying elements like  $^{90}\text{Sr}$  and  $^{137}\text{Cs}$ . For the evaluation of antineutrino emissions, we obtained the isotopic concentrations of radioactive isotopes in spent fuel discharged from a pressurized water reactor, PWR, using a simulation with the reactor simulation code SERPENT2 [15]. A burn-up of 55 MWd/kg and a uranium enrichment of 4% was implemented. We then used the beta spectra of all beta-decaying nuclides and converted them to the antineutrino spectra shown in figure 1 for different ages of the nuclear waste.

The antineutrinos are emitted at low energies with the emission significantly decreasing at 2.3 MeV. The maximum energy is reached at 4.3 MeV with an emission rate more than ten orders of magnitude smaller than for the lower energy range up to 2.3 MeV. Considering the detection via IBD with its threshold at 1.8 MeV, the energy region that can be detected is fairly small. In this

region, the antineutrino emission is dominated by the decay of the  $^{90}\text{Y}$  isotope, which is a decay product of the highly abundant fission product  $^{90}\text{Sr}$  and stays in equilibrium with it.

In the Appendix A an exemplary scenario of a monitoring application for a geological repository is shown. It presents the expected event rates in an active medium of Tetra-Methyl-Silane.

### 3 Liquid-organic time projection chamber

The TPC is a widely used tracking detector due to its good track reconstruction ability and energy loss resolution. It usually consists of a large detection volume where particles leave energy depositions of electrons through ionization. Due to an externally applied electric field the ionization electrons drift towards an anode plane. A three-dimensional reconstruction is provided by a segmented, two-dimensional readout at the anode and the measurement of the drift time of the electrons.

Originally, TPCs use a gas mixture as sensitive material to measure the passage of charged particles. The neutral neutrino cannot be detected directly by an ionization detector, but charged final state particles from neutrino interactions with the detector material can be measured. Due to the extremely small cross section of neutrino interactions, a denser material than a gas is necessary. Shortly after the invention of the gaseous TPC, the usage of liquid argon as active medium was suggested because of its higher density [16]. Nowadays, using liquefied noble gases has become an established technology for the detection of weakly interacting particles. In neutrino experiments like MicroBooNE [17] and ArgonNeuT [18] liquid argon TPCs have been exploited, whereas liquid xenon is used in dark matter searches, e.g. the experiments XENON100 [19], LUX [20] and PandaX [21]. Currently, the DUNE neutrino experiment builds huge liquid argon TPCs for its far detector with a combined 70 kiloton of liquid argon as the target mass [22]. First results with this technology were gained at the ProtoDUNE setup of the CERN neutrino platform [23].

One drawback of liquid noble gases is that they need to be cooled down by a cryogenic system and therefore, it is very challenging to construct and operate a detector system with this technology. Hence, studying alternative high-density media that allow drifting electrons at room temperatures has been of special interest for a long time. One promising material is Tetra-Methyl-Silane, TMS, which is a non-polar organic liquid with spherically shaped molecules. Its usage in ionization detectors has been previously investigated [24] with the focus on its application in calorimetry. For example, KASCADE-Grande [25] used liquid ionization chambers filled with TMS in their central calorimeter. In recent years, the use of these organic liquids as sensitive material of a TPC has been discussed [12, 13]. By operating small test chambers, the charge transport in organic liquids has been studied by measuring the charge yield [26], the drift velocity [27] and the mean free drift length [28]. Still, these studies have to be intensified as open questions remain. For instance, further parameters relevant for the electron drift in organic liquids, such as the diffusion coefficients, still have to be investigated.

Another advantage of an organic liquid with respect to liquid noble gases is the presence of free protons due to its hydrogen content. Through this, a low threshold for the IBD process can be reached, making it possible to detect antineutrinos down to the energy of 1.8 MeV. Event rates should also be comparable with liquid scintillation detectors. For example, the number of target nuclei for IBD in TMS is as large as 81 % of the one in the scintillator material of KamLAND [29].

**Table 1.** Simulation parameters for the two detector configurations. In both cases a high voltage of 500 kV and a sensitive volume of  $80 \text{ m}^3$  is assumed.

	Detector 1	Detector 2
maximum drift length $l$	1 m	10 m
electric field $E$	5.0 kV/cm	0.5 kV/cm
drift velocity $v_d$	$5.5 \mu\text{m/ns}$	$0.5 \mu\text{m/ns}$
diffusion coefficients $d_{L,T}$	$60 \mu\text{m}/\sqrt{\text{cm}}$	$190 \mu\text{m}/\sqrt{\text{cm}}$
electron yield $G_{if}$	$7 e^-/\text{keV}$	$5 e^-/\text{keV}$

#### 4 Simulation setup and event generation

In order to investigate the reconstruction of IBD events in a liquid-organic (LOr) TPC, we simulated antineutrino interactions within Tetra-Methyl-Silane as target material using the event generator GENIE [30] and the energy spectrum of figure 1 at 100 years. Since the flux effectively vanishes above 2.3 MeV, IBD can only take place at the hydrogen nuclei. The outgoing positron and neutron from the IBD reaction are then fed to a GEANT4 [31] simulation to investigate their interaction with TMS. From this simulation we obtain the energy deposition of each particle. These are then translated into the number of electrons with an estimated electron yield  $G_{if}$  that are used to simulate the spatial charge distribution at an anode with a readout structure of squared pads with a size of  $5 \text{ mm} \times 5 \text{ mm}$  considering the drift velocity  $v_d$  and the diffusion coefficient for longitudinal  $d_L$  and transverse diffusion  $d_T$ .

We examine two extreme, but still reasonable detector configurations with different maximum drift lengths of  $l_1 = 1 \text{ m}$  and  $l_2 = 10 \text{ m}$ , respectively, where we keep a sensitive volume of  $80 \text{ m}^3$  congruous to our study presented in the Appendix A. For both configurations we assume a cathode high voltage of  $-500 \text{ kV}$  which generates a drift field of  $E_1 = 5 \text{ kV/cm}$  and  $E_2 = 0.5 \text{ kV/cm}$ , respectively. For the first detector configuration, Detector 1,  $G_{if,1} = 7 e^-/\text{keV}$  [32] and  $v_{d,1} = 5.5 \mu\text{m/ns}$  [28] are used. For the second configuration, Detector 2, we assume  $G_{if,2} = 5 e^-/\text{keV}$  and  $v_{d,2} = 0.5 \mu\text{m/ns}$  using a mobility of  $\mu = 105 \text{ cm}^2/\text{V/s}$  [33].

Due to the lack of experimental data, we use the Einstein Relation  $D_{L,T} = \mu \cdot k_B T / e$  to estimate the thermal limit of the diffusion coefficient  $D_{L,T}$  with given mobility  $\mu$ . To express the diffusion as a function of the drift distance  $l_d$  instead of drift time  $t_d$  via the formula  $\sigma = \sqrt{D_{L,T} \cdot t_d} = d_{L,T} \sqrt{l_d}$  we transform the diffusion coefficient using equation 4.1:

$$d_{L,T} = \sqrt{\frac{2D_{L,T}}{v_d}} = \sqrt{\frac{2k_B T}{eE}}. \quad (4.1)$$

Measurements of electron diffusion in liquid argon show that the actual diffusion coefficient  $D_{L,T}$  is a factor 3–4 larger than the thermal limit [34]. Assuming a factor 4 for TMS we get a diffusion coefficient of  $d_{L,T,1} \approx 60 \mu\text{m}/\sqrt{\text{cm}}$  for Detector 1 and  $d_{L,T,2} \approx 190 \mu\text{m}/\sqrt{\text{cm}}$  for Detector 2. We use the maximum drift length to study the maximum impact of diffusion. A summary of the simulation parameters can be found in table 1.

With these detector scenarios we want to evaluate two extreme, but still reasonable combinations of electric field and drift lengths. Detector 1 has a higher electric field which comes with a higher

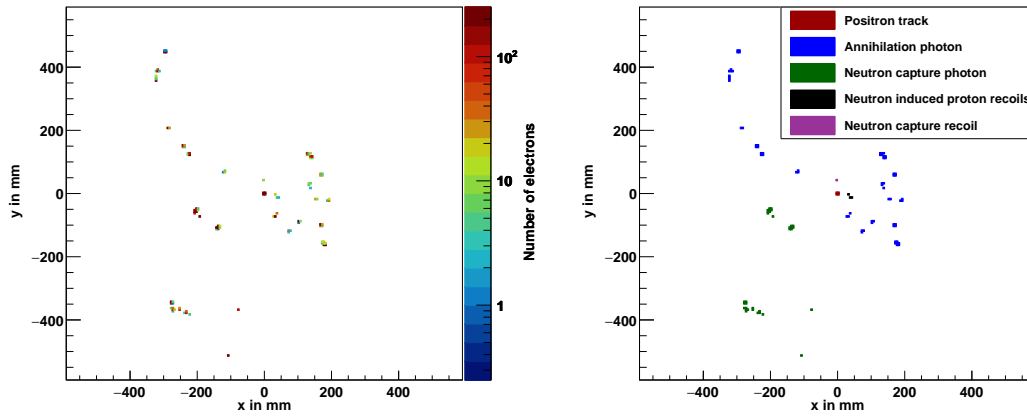


**Figure 2.** Simulation of an IBD event projected onto the anode for the Detector 1 scenario. The left side shows the distribution of the single electrons in a color-coded scale. The right side shows which particle is associated to the ionization clusters.

drift velocity and smaller diffusion coefficient. Detector 2 on the other hand has a larger drift length which results in less readout channels when keeping the same sensitive volume. Both scenarios are limited by the maximum manageable high voltage for which we consider 500 kV. Another important point that has to be kept in mind is that in liquids, organics or cryogenic noble gases, high purity is needed to reach a sufficient free electron lifetime. For TMS this electron lifetime is constant for electric fields below  $E = 20 \text{ kV/cm}$  according to [35]. With the drift velocity rising proportional to the electric field a balance needs to be found between electric field and drift length.

## 5 Inverse beta decay signature in a LOr-TPC

Figure 2 shows the interaction of an antineutrino entering the TPC perpendicular to the drift direction for detector configuration 1. Integrated over the whole event time, it shows all energy depositions of the secondary particles. On the left side, for each readout pad the recorded ionization in number of electrons is shown. On the right side, the associated particle is mapped to each of the ionization clusters. Contrary to liquid scintillation detectors, which can only distinguish a prompt from a delayed signal, here also the ionization of the positron and the scattering of the neutron is directly accessible.

For the comparison of the detector configurations, figure 3 depicts a zoomed view into the projected charge distributions simulated for the same event with the respective drift parameters. It shows the ionization cluster of the positron in the center, the ionization from the neutron-induced proton recoils on the right, the neutron capture recoil on top and some ionization of one of the annihilation photons on the bottom right. For Detector 2 that is shown on the right side of figure 3, the charge clusters are spread over more pads as expected due to the larger diffusion coefficient and the longer drift distance. As result, the clusters of the positron and the neutron ionization are more likely to overlap and therefore, lead to a poorer separation. In addition, the larger spread of the charge reduces the potential electric pad signals that are especially low for the small ionization signals of the proton recoils which is slightly lower for Detector 2.

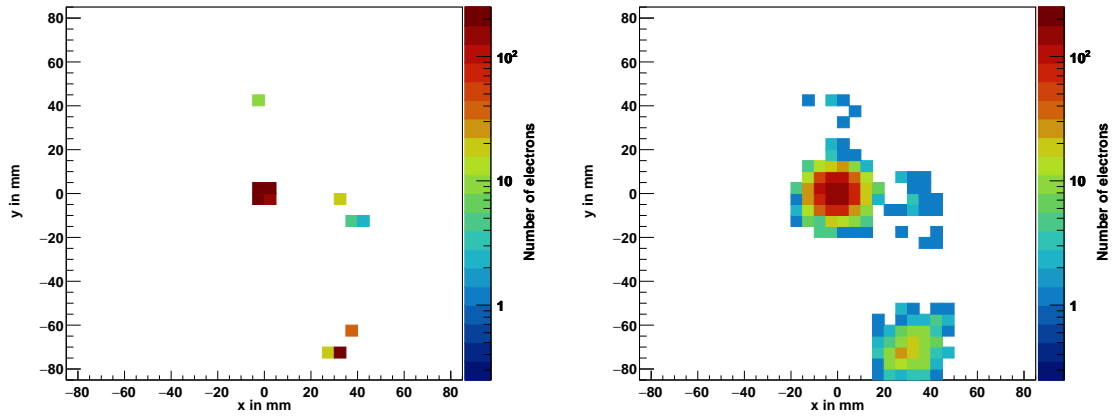


**Figure 3.** Comparison between the two detector configurations using the same event. The charge distribution of Detector 1 is shown on the left side. The right side shows the distribution of Detector 2. Both show the same zoomed-in view in the center of the event also shown in figure 2.

We will explain each signal created by the particles of the IBD final state in the following. The numbers are given for Detector 1 first and for Detector 2 in brackets behind. In the simulated energy region, the positron receives a kinetic energy smaller than 0.5 MeV. This leads to a typical track length below 1 mm before annihilation. This track starts at the primary vertex of the IBD interaction and can be clearly identified by the up to 3200 (2286) electrons that are created along its path. The ionization released along the positron track is a direct measure of the positrons' initial kinetic energy, which in turn measures the energy of the antineutrino as depicted in figure 4.

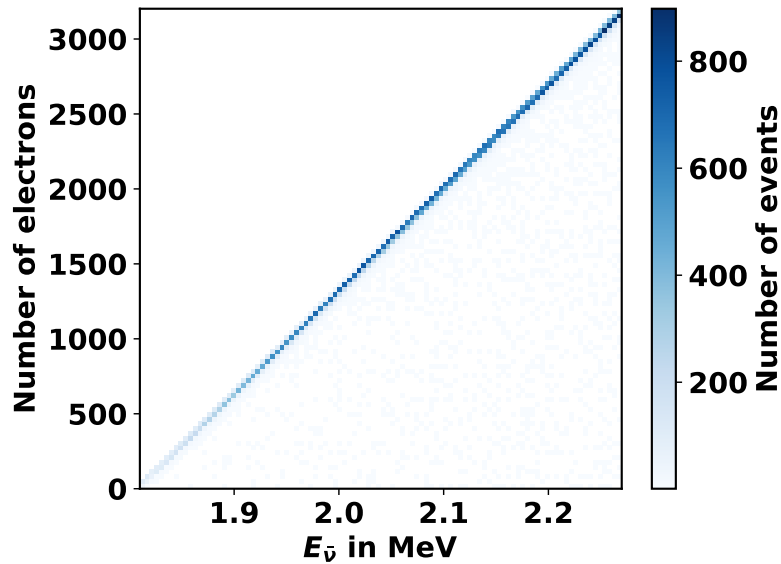


**Figure 4.** Number of ionization electrons created by the positron track in Detector 1 as function of the antineutrino energy.



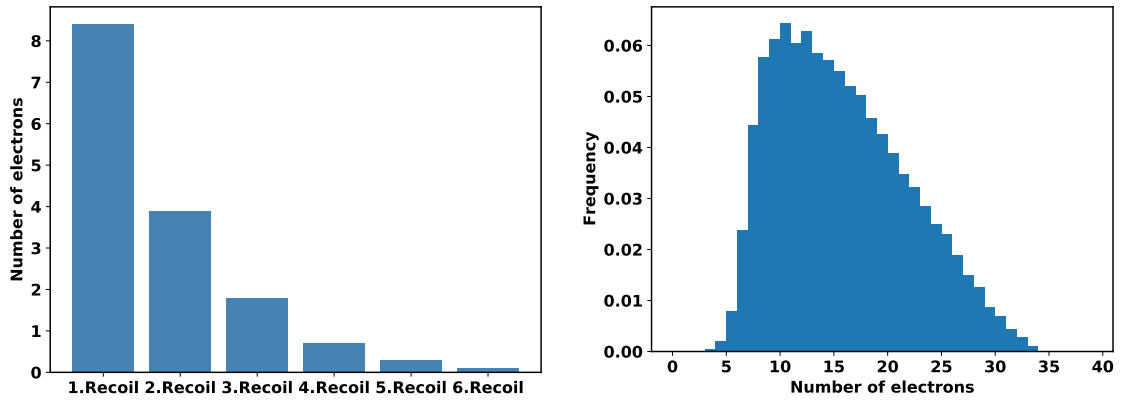


**Figure 5.** Number of electrons created by neutron-induced proton recoils in Detector 1. The left side shows the number of electrons created in each proton recoil. The right side shows the integrated number of electrons from proton recoils in each IBD event.

In rest, the positron annihilates with an electron of the detector material and two 511 keV photons are created which can be used as a prompt signal to identify the IBD event as also done in liquid scintillation detectors. As shown in the event display, these photons produce characteristic energy depositions due to the fact that they initially travel a few centimeters losing their energy by Compton scattering before the final photo effect takes place.

During its propagation, the neutron scatters off the nuclei of the detector liquid until it is thermalized and finally captured. The nucleon created by the neutron capture is produced in an excited state and finally releases the excitation energy via photon emission. From 100,000 simulated events we found that in 93 % of the cases the neutron is captured by a hydrogen nucleus which releases a single photon of 2.2 MeV energy. Again, this photon loses its energy by Compton scattering, traversing the liquid for a few centimeters. If the neutron is captured by another nucleus of the detector liquid, several photons can be emitted with energies according to the excitation levels of the produced nucleus. On average it takes  $(244.2 \pm 1.2) \mu\text{s}$  until the neutron is captured and the photon is released. Detecting the photon from the neutron capture process in addition to the positron annihilation photons gives a clear event signature.

The neutron produced by the IBD has typical kinetic energies between 1 keV and 3 keV due to its larger mass compared to the positron. Therefore, the positron obtains practically all of the energy of the incoming antineutrino. At the IBD energy threshold, the positron receives no kinetic energy and since the proton is at rest before the interaction, the neutron takes over the complete momentum of the antineutrino. Hence, it also has the identical direction as the incoming antineutrino. With increasing neutrino energy and thus rising positron momentum, the deviation between neutron and antineutrino direction increases due to momentum conservation [36]. Still, the neutron direction is largely correlated with the antineutrino direction at the considered energies.

Afterwards, the neutron changes its direction due to scattering from the protons in the detection material. The mean distance between the antineutrino vertex and the first neutron-induced proton recoil is  $(9.20 \pm 0.04) \text{ mm}$ . Usually, the largest energy transfer occurs in the first collision. It decreases with each collision as shown on the left side of figure 5. The first proton recoil creates

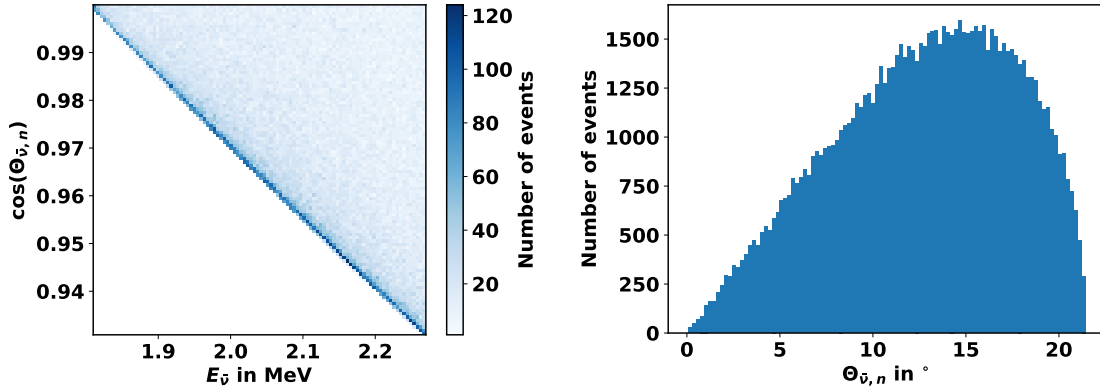


**Figure 6.** Angular distribution of the neutron as a function of the incident antineutrino direction. The left side shows the angular deviation as a function of the antineutrino energy. The right side shows the angular probability distribution of IBD events based on the nuclear waste spectrum that we consider.

on average 8.4 (6) electrons while it is only 3.9 (2.8) for the second and 1.8 (1.3) for the third. As the right side of figure 5 shows, in each event an integrated signal of 5–30 (4–21) electrons can be expected from the neutron-induced proton recoils. The most probable value is around 10 (7).

The various physical processes discussed so far yield very different amounts of ionization to be detected. Especially the detection of the neutron signal consists of only a few electrons and is therefore very challenging, but could be realized using the concept of a dual-phase TPC. Here, adding a gaseous layer on top of the liquid drift volume allows for electron amplification in the gas due to an avalanche process induced by a high electric field applied in this region. This concept of dual-phase TPCs has been successfully achieved in liquid xenon TPCs for dark matter searches [37] and in the Protodune detector [38].

## 6 Investigations on the reconstruction of the antineutrino direction

An additional benefit of the full reconstruction of IBD final states could be the access to information on the initial direction of the detected antineutrino on an event-by-event basis.

We investigated IBD events simulated with GENIE for the nuclear waste antineutrino spectrum. The left side of figure 6 shows the angle between the incident antineutrino direction and the initial direction of the neutron as function of the antineutrino energy. Directly at the IBD threshold, the initial neutron direction is identical to the incident antineutrino direction. For higher antineutrino energies  $E_\nu$  the deviation between the neutron and antineutrino direction increases. The maximum angle can be described analytically, see equation 6.1 [36].

$$\cos \phi_{\max} = \frac{\sqrt{2E_\nu \Delta - (\Delta^2 - m_e^2)}}{E_\nu} \quad \text{with } \Delta = m_n - m_p. \quad (6.1)$$

Since the most probable angle between neutron and antineutrino corresponds to the maximum angle (as can be seen in figure 6), the neutron is initially directed in a cone around the antineutrino direction. Later the neutron undergoes several scattering events. The correlation with the initial

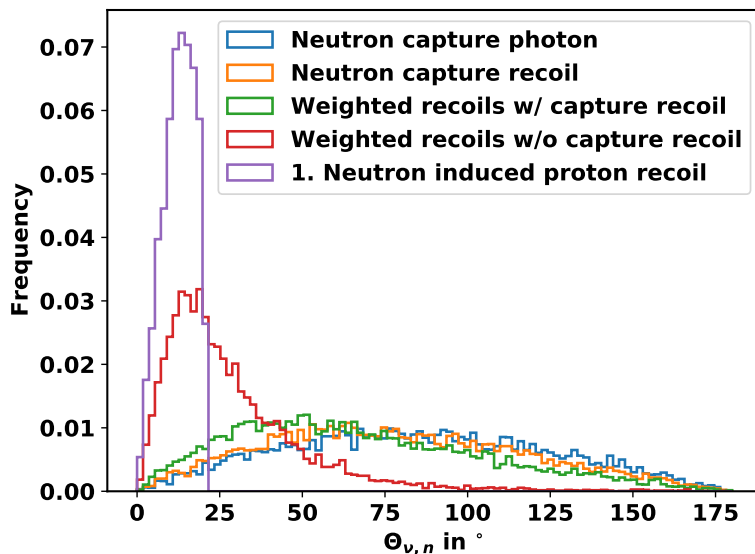


**Figure 7.** Angle between reconstructed neutron direction and incident antineutrino direction. Distributions are shown for different reconstruction methods, as explained in the text.

neutron direction and the antineutrino direction is reduced by each scattering process. Therefore, it would be desirable to reconstruct the location of the first or of the first few neutron-proton scatterings. The connecting line between this location and that of the positron track would then yield a very good prediction of the direction of the antineutrino.

On the right side of figure 6, the angle between the neutron and antineutrino direction is shown for the IBD events based on the nuclear waste antineutrino spectrum considered by us. The maximum angle is  $21^\circ$  and the distribution peaks at around  $15^\circ$ .

Furthermore, we studied the potential to reconstruct the antineutrino direction via the energy depositions using our GEANT4 Monte Carlo simulation. In this study, we considered five different definitions for a neutron direction vector that always starts at the IBD interaction origin and compared it with the incident antineutrino direction vector. We investigated (1) the first neutron-induced proton recoil, (2) the energy-weighted mean of all proton recoil ionization clusters, (3) all recoils including that of the nucleus capturing the neutron, (4) only the recoil of the nucleus capturing the neutron, and (5) the ionization of the first Compton-scatter of the photon released after the neutron capture. As depicted in figure 7, the angular correlation between the direction of the initial antineutrino and the different definitions (1-5) diminishes significantly with more ionization energy taken into account. For (4) and (5) the distributions even become isotropic, so these events can not be used to reconstruct the direction on a event basis. Therefore, we conclude that for the best possible reconstruction of the antineutrino direction only the first neutron-induced proton recoil should be considered. However, as it might not be possible in all cases to isolate this energy cluster from the signature arriving at the anode, the second best option would be to use the energy-weighted position of all proton recoils without the recoil of the capturing nucleus. As we have already shown above, the deposited energy on average decreases with each neutron scattering. Hence, automatically only

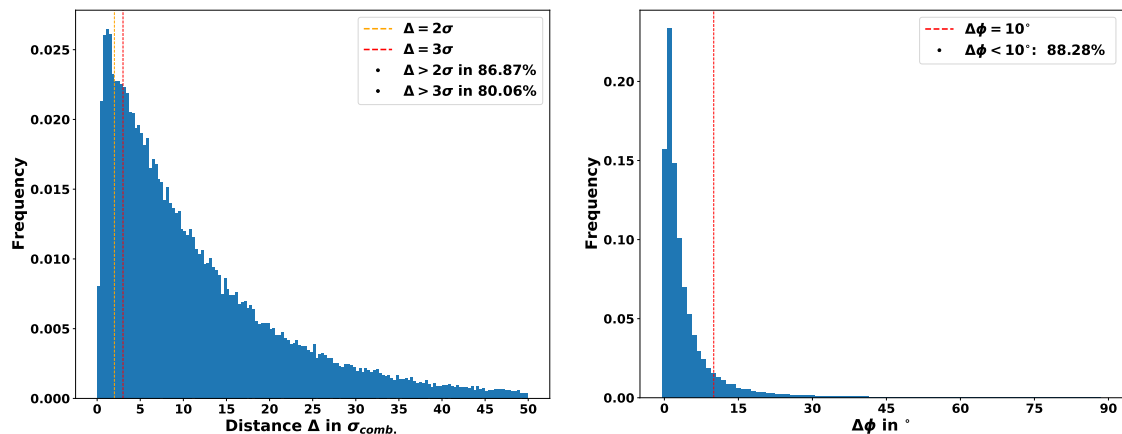


**Figure 8.** Distance of the charge distributions of neutron and positron on an anode for Detector 1 in combined standard deviations on the left side. On the right side the resulting angular deviation of the reconstructed and the true neutron direction for events with more than two combined standard deviation is shown. Here only the charge cluster of the first neutron-induced proton recoil was used.

the first few recoils will result in an measurable energy deposition and would be taken into account. As our simulations show, the capture recoil is usually  $\Delta t \approx 240 \mu\text{s}$  delayed and can therefore be excluded from the other proton recoils.

Finally, we studied the reconstruction of the neutron direction from the charge distribution created by the drifting electrons at an anode using the drift simulation described above. The question we pose is to which extent the neutron recoil cluster(s) can be separated spatially from the positron track, identifying them as small satellite clusters. Since the positron track is rather short, it can also be considered as a single ionization cluster from which we determine the center of charge and its two-dimensional standard deviation. We then determine the same for both the ionization clusters of all neutron-induced recoil protons and for only the first one. For IBD events where the antineutrino direction is perpendicular to the drift direction of the LOr-TPC we found that for 87 % of the events, the charge distributions are more than two combined standard deviations apart in the Detector 1 scenario as depicted in figure 8 using only the first neutron-induced proton recoil. For 88 % of these events, the neutron direction can be reconstructed with a deviation of less than  $10^\circ$  from the true neutron direction. When using all proton recoils for the neutron reconstruction, only 72 % have a deviation of more than two combined standard deviation. In 68 % of these events, the neutron direction can be reconstructed with less than a  $10^\circ$  deviation.

For Detector 2, the charge distributions are only separated for 29 % of the events with more than two standard deviations considering only the first neutron-induced proton recoil. From these events, 54 % can be reconstructed with less than  $10^\circ$  deviation. In case the charge distribution is reconstructed by all proton recoils 33 % of the events are more than the two standard deviations apart in this scenario, of which 55 % can be reconstructed with less than  $10^\circ$  deviation.

Detector 1 shows much better performance than Detector 2. For example, assuming a detector volume of dimensions  $10 \times 4 \times 2 \text{ m}^3$ , the Detector 1 setup with the 1 m maximum drift length can be realized by a central cathode in parallel to the  $10 \times 4 \text{ m}^2$  large side. This setup would require a

total readout area of  $80 \text{ m}^2$ . The Detector 2 setup could be realized with a cathode on one of the  $2 \times 4 \text{ m}^2$  large sides. In summary, Detector 1 delivers better results due to the ten times shorter drift length, but needs a ten times larger readout area instrumented.

## 7 Conclusion and Outlook

We presented the first comprehensive simulation-based study of the expected IBD signatures in a liquid-organic TPC. This is a newly proposed detection method for neutrino scattering events using a liquid-organic TPC which aims for a full reconstruction of the IBD final state. The identification of this unequivocal event signature has the potential to enable a background-minimized detection of antineutrino events. The basis for this is the reconstruction of the positron track. On the one hand, it improves the neutrino energy resolution due to the correlation of ionization of the positron track to the initial antineutrino energy. On the other hand, it makes it possible to distinguish the IBD events containing a positron signal plus two annihilation photons from background events involving  $\beta$ -electrons.

Our simulation studies are an initial assessment. Based on our results, we conclude that it could be possible to indeed associate the energy depositions to the final state particles and achieve a complete reconstruction of IBD events. Further studies on the identification with dedicated reconstruction algorithms have to be performed. Recent advances in these analysis techniques are promising in this respect.

In addition, we showed that the direction of the incoming antineutrino could be estimated from the locations of the energy depositions caused by the recoil protons produced by the scattering of the final state neutrons. Even though their ionization signal is very small, it might be detectable as a satellite cluster to the positron track. Experimental studies have to be undertaken to decide whether this is achievable, given the fact that the positron track's signal is two orders of magnitude larger than that of the recoil protons. This concept could lead to a measurement of the antineutrino direction on an event-by-event basis, even when our simulations show that not all proton recoils have a sufficient distance from the positron track. It would in any case, however, be a large improvement compared to current capabilities using scintillation detectors.

Future simulation studies should also address signatures for antineutrinos entering the detector in parallel to the electron drift direction. Here, the neutrons and positron tracks would be much closer together in the anode plane. How they could be distinguished in a three dimensional reconstruction also using the drift time measurement should be further assessed.

We will soon start further studies based on a TPC prototype to confirm the results from simulation studies described in this paper. We intend to measure drift velocity, electron lifetime and the diffusion parameters of TMS.

### A Initial study for monitoring a geological repository with a liquid-organic TPC

As an initial study we investigated a model loosely related to the now discarded Gorleben site [39] in Germany. It comprises 2240 containers with ten spent fuel assemblies each. The production year of the fuel was simulated corresponding to the German program, though we assumed the last fuel to be discharged in 2020.

**Table 2.** Expected detection rates of the antineutrino emissions without background evaluated with a detector volume of 80 m<sup>3</sup> TMS in a TPC.

Time elapsed since 2020 in years	Number of IBD events detected in 3 months
10	761
25	532
50	293
100	89
125	49
150	27

The layout foresaw the storage caverns to be located at a depth of 870 m. In our assessment, we envisaged that an antineutrino detector would be placed at the same depth as the repository, but 50 m away from the outermost containers. In view of the transportation and deployment requirements, we considered a detection volume of 80 m<sup>3</sup> of Tetra-Methyl-Silane for the antineutrino detector. The results of this preliminary study are summarised in table 2. It can be seen that the expected detection rate diminishes significantly with time due to the decay of <sup>90</sup>Sr. Note that larger detectors or multiple detectors at different locations could be employed, including above the repository. These results show that antineutrino monitoring with a liquid-organic TPC could be possible, but indeed only using a detection technique with high background suppression.

## Acknowledgments

We thank Madalina Wittel for her engagement in starting this project and we acknowledge the contributions of David Betram, Helge Haveresch, Anike Ohm and Hagen Weigel. The project was funded by the Federal Ministry of Education and Research (BMBF) and the Ministry of Culture and Science of the German State of North-Rhine Westphalia (MKW) under the Excellence Strategy of the Federal Government and the Länder. Malte Götttsche and Thomas Radermacher are generously funded by the VolkswagenStiftung Freigeist Fellowship.

## References

- [1] R. Carr et al., *Neutrino-Based Tools for Nuclear Verification and Diplomacy in North Korea*, *Science & Global Security* **27** (2019) 15–28.
- [2] E. Christensen et al., *Antineutrino Monitoring for Heavy Water reactors*, *Phys. Rev. Lett.* **113** (2014) 042503.
- [3] M. Askins et al., *The Physics and Nuclear Nonproliferation Goals of WATCHMAN: A Water Cherenkov Monitor for Antineutrinos*, [arXiv/1502.01132](https://arxiv.org/abs/1502.01132).
- [4] V. Brdar, P. Huber and J. Kopp, *Antineutrino Monitoring of Spent Nuclear Fuel*, *Phys. Rev. Applied* **8** (2017) 054050.
- [5] M. Wittel and M. Götttsche, *Antineutrino Detection Techniques for Monitoring Long-Term Geological Repositories*, *ESARDA Bulletin* **60** (2020) 20–27.

- [6] J. Ashenfelter et al., *First Search for Short-Baseline Neutrino Oscillations at HFIR with PROSPECT*, *Phys. Rev. Lett.* **121** (2018) 251802.
- [7] H. Almazán et al., *Accurate Measurement of the Electron Antineutrino Yield of U235 Fissions from the STEREO Experiment with 119 Days of Reactor-On Data*, *Phys. Rev. Lett.* **125** (2020) .
- [8] H. de Kerret et al., *The Double Chooz antineutrino detectors*, [arXiv/2201.13285](https://arxiv.org/abs/2201.13285).
- [9] F. An et al., *The detector system of the Daya Bay reactor neutrino experiment*, *Nucl. Instrum. Meth. A* **811** (2016) 133–161.
- [10] J. Ahn et al., *RENO: An Experiment for Neutrino Oscillation Parameter  $\theta_{13}$  Using Reactor Neutrinos at Yonggwang*, [arXiv/1003.1391](https://arxiv.org/abs/1003.1391).
- [11] M. Agostini et al., *Comprehensive geoneutrino analysis with Borexino*, *Phys. Rev. D* **101** (2020) 012009.
- [12] N. McConkey and Y. Ramachers, *Liquid Scintillator Time Projection Chamber Concept*, *Nucl. Instrum. Meth. A* **718** (2013) 459–461, [[arXiv/1205.5695](https://arxiv.org/abs/1205.5695)].
- [13] J. Dawson and D. Kryn, *Organic Liquid TPCs for Neutrino Physics*, *JINST* **9** (2014) P07002, [[arXiv/1405.1308](https://arxiv.org/abs/1405.1308)].
- [14] E. Caden, *Studying Neutrino Directionality with Double Chooz*, [arXiv/1208.3628](https://arxiv.org/abs/1208.3628).
- [15] J. Leppänen et al., *The Serpent Monte Carlo Code: Status, Development and Applications in 2013*, *Annals of Nuclear Energy* **82** (2014) 06021.
- [16] C. Rubbia, *The Liquid Argon Time Projection Chamber: A New Concept for Neutrino Detectors*, CERN-EP-INT-77-08, CERN-EP-77-08 (1977) .
- [17] R. Acciarri et al., *Design and construction of the MicroBooNE detector*, *JINST* **12** (2017) P02017–P02017.
- [18] C. Anderson et al., *The ArgoNeuT detector in the NuMI low-energy beam line at fermilab*, *JINST* **7** (2012) P10019–P10019.
- [19] E. Aprile et al., *The XENON100 dark matter experiment*, *Astroparticle Physics* **35** (2012) 573–590.
- [20] D. Akerib et al., *The Large Underground Xenon (LUX) experiment*, *Nucl. Instrum. Meth. A* **704** (2013) 111–126.
- [21] X. Cao et al., *PandaX: A Liquid Xenon Dark Matter Experiment at CJPL*, *Sci. China Phys. Mech. Astron.* **57** (2014) 1476–1494, [[arXiv/1405.2882](https://arxiv.org/abs/1405.2882)].
- [22] R. Acciarri et al., *Long-Baseline Neutrino Facility (LBNF) and Deep Underground Neutrino Experiment (DUNE): Conceptual Design Report, Volume 1: The LBNF and DUNE Projects*, FERMILAB-DESIGN-2016-01 (2016) , [[arXiv/1601.05471](https://arxiv.org/abs/1601.05471)].
- [23] B. Abi et al., *First results on ProtoDUNE-SP liquid argon time projection chamber performance from a beam test at the CERN Neutrino Platform*, *JINST* **15** (2020) P12004–P12004.
- [24] A. Gonidec et al., *Ionization chambers with room temperature liquids for calorimetry*, CERN-EP-88-36 (1988) .
- [25] J. Engler et al., *A warm-liquid calorimeter for cosmic-ray hadrons*, *Nucl. Instrum. Meth. A* **427** (1999) 528–542.
- [26] M. Farradèche et al., *Free ion yield of trimethyl bismuth used as sensitive medium for high-energy photon detection*, *JINST* **13** (2018) P11004–P11004.

- [27] H. Faidas, L. Christophorou and D. McCorkle, *Drift velocities of excess electrons in 2,2,4,4-tetramethylpentane and tetramethylsilane: A fast drift technique*, *Chem. Phys. Lett.* **163** (1989) 495–498.
- [28] S. Wu et al., *A Tetramethylsilane TPC with Cherenkov light readout and 3D reconstruction*, *Nucl. Instrum. Meth. A* **972** (2020) 163904.
- [29] S. Abe et al., *Precision Measurement of Neutrino Oscillation Parameters with KamLAND*, *Phys. Rev. Lett.* **100** (2008) .
- [30] C. Andreopoulos et al., *The GENIE Neutrino Monte Carlo Generator*, *Nucl. Instrum. Meth. A* **614** (2010) 87–104, [[arXiv/0905.2517](#)].
- [31] S. Agostinelli et al., *Geant4—a simulation toolkit*, *Nucl. Instrum. Meth. A* **506** (2003) 250–303.
- [32] R. Holroyd, *Electrons in nonpolar liquids*, in *Charged Particle and Photon Interactions with Matter*, pp. 175–206, Taylor&Francis Group, 2002. [DOI](#).
- [33] J. Engler, *Liquid ionization chambers at room temperatures*, *J. Phys. G: Nucl. Part. Phys.* **22** (1996) 1–23.
- [34] Y. Li et al., *Measurement of longitudinal electron diffusion in liquid argon*, *Nucl. Instrum. Meth. A* **816** (2016) 160–170.
- [35] M. Lopes, K. Masuda and T. Doke, *Estimation of the electron lifetime in tetramethylsilane*, *Nucl. Instrum. Meth. A* **271** (1988) 464–470.
- [36] P. Vogel and J. Beacom, *Angular distribution of neutron inverse beta decay  $\bar{\nu}_e + p \rightarrow e^+ + n$* , *Phys. Rev. D* **60** (1999) 053003.
- [37] M. Schumann, *Dual-Phase Liquid Xenon Detectors for Dark Matter Searches*, *JINST* **9** (2014) C08004, [[arXiv/1405.7600](#)].
- [38] J. Dawson, *Status of ProtoDUNE dual phase*, *J. Phys.: Conf. Ser.* **1312** (2019) 012004.
- [39] W. Bollingfehr et al., *Endlagerkonzepte - Bericht zum Arbeitspaket 5*, *GRS* **272** (2011) .